Volume 1 | Number 1 | Jan 2013 | Pages 1–100

Nanoscale

www.rsc.org/nanoscale

ROYAL SOCIETY OF CHEMISTRY

ROYAL SOCIETY OF CHEMISTRY

www.rsc.org/nanoscale

Controlled Synthesis and Photocatalysis of Sea Urchin-Like

Fe$_3$O$_4$@TiO$_2$@Ag Nanocomposite

Yilin Zhao, Chengran Tao, Gang Xiao, Guipeng Wei, Linghui Li, Changxia Liu, Haijia Su*
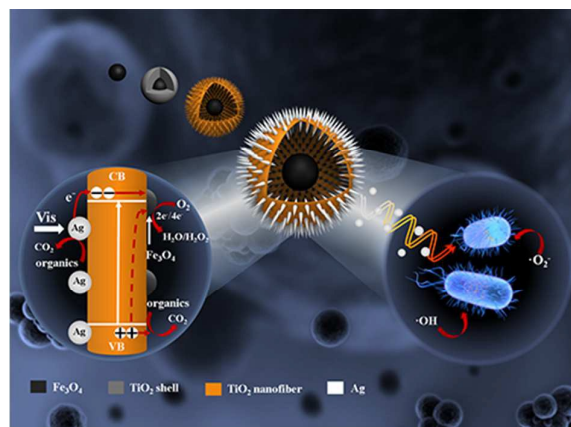
Based on the synergistic photocatalytic activities of nano-sized TiO$_2$ and Ag, as well as the magnetic property of Fe$_3$O$_4$, a sea urchin-like Fe$_3$O$_4$@TiO$_2$@Ag nanocomposite (Fe$_3$O$_4$@TiO$_2$@AgNCs) is controllably synthesized with tunable cavity size, adjustable shell layer of TiO$_2$ nanofiber, higher structural stability and larger specific surface area. Here, Fe$_3$O$_4$@TiO$_2$@AgNCs are obtained with Fe$_3$O$_4$ as core and nanofiber TiO$_2$/Fe$_3$O$_4$/Ag nanoheterojunctions as shell; and Ag nanoparticles with diameter of approximately 4 nm are loaded both on TiO$_2$ nanofibers and inside the cavities of sea urchin-like Fe$_3$O$_4$@TiO$_2$ nanocomposites uniformly. Ag nanoparticles leads to the production of more photogenerated charges in

Beijing Key Laboratory of Bioprocess, Beijing University of Chemical Technology (BUCT)

15 BeiSanhuan East Road, ChaoYang District, Beijing, 100029, P. R. China

E-mail: suhj@mail.buct.edu.cn, Tel.: +86-10-64452756, Fax.: +86-10-64414268

1    $TiO_2/Fe_3O_4/Ag$ heterojunction via LSPR absorption, and enhances band-gap absorption of TiO_2,

2   while Fe_3O_4 cocatalyst provides as active sites for oxygen reduction by the effective transfer of

3   photogenerated electrons to oxygen. So the photocatalytic performance is improved due to the

4   synergistic effect of synergistic effect of $TiO_2/Fe_3O_4/Ag$ nanoheterojunctions. As photocatalysts

5   under UV and visible irradiation, the as-synthesized nanocomposites display enhanced

6   photocatalytic and recycling properties for the degradation of Ampicillin. Moreover, they present

7   better broad-spectrum antibiosis under visible irradiation. The enhanced photocatalytic activity and

8   excellent chemical stability, in combination with the magnetic recyclability, make this

9   multifunctional nanostructure promising a candidate for antibiosis and remediation in aquatic

10   environmental contamination in the future.

11   **Keywords:** Sea urchin-like $Fe_3O_4@TiO_2@Ag$ nanocomposites, magnetic materials, controllable

12   preparation, photocatalytic activities under visible irradiation, recycling properties.

13   **1. Introduction**

14   Since the discovery of the phenomenon of photocatalytic splitting of water under ultraviolet light by

15   Fujishima and Honda in 1972,[1]titanium dioxide (TiO_2), as an interesting semiconductor material,

16   has been widely investigated for environmental applications because of its chemical inertness,

17   strong oxidizing power, cost effectiveness, and long term stability against photo- and chemical

18   corrosion. [2,3]Its wide band gap energy(Eg)3.0–3.2 eV, allows the absorption of UV light and the

19   generation of electrons (e−) and holes (h+), which subsequently provides a favorable condition for

20   red-ox reactions. [4] It has been determined that a highly crystalline structure for TiO_2 material is

21   essential to enhance the generation and migration of photo generated electrons/holes.[5,6] On the other

1 hand, the photocatalytic activity of TiO_2 is related with its size, shape, surface area, morphology,

2 and dimensionality.[5] Nanometer-scaled TiO_2 based catalysts, such as nanoparticles, nanorods,

3 nanosheets, and nanotubes, exhibit promising photocatalytic performance, but they tend to

4 aggregate during the photocatalysis process, and therefore reduce their active surface area.[2]

5 Many studies found that three-dimensional (3D) hierarchical nanoarchitecture assemblies of

6 one dimensional (1D) nanostructures, including nanorods, nanowires, and nanotubes, are highly

7 desired due to their high surface-to-volume ratio, high organic pollutant adsorption, and excellent

8 incident light scattering within the structures.[7-10] Similarly, flower-like multineedle TiO_2

9 nanostructures were successfully fabricated by mild aqueous chemistry.[11,12] An alternative approach

10 for producing high-surface-area anatase materials is the creation of mesoscale porosity in such

11 materials. The synthesis of mesoporous structures has been most extensively reported.[4, 13-15]

12 Finely dispersed TiO_2 particles have a large reactive surface area, but it is difficult to separate

13 and recover them from liquid phase. The recovery and reusability of TiO_2 particles are, however,

14 crucial for their further applications. Conventional separation methods, including centrifugation and

15 filtration, may lead to catalyst loss and energy consumption. Even though photocatalysts fixed on

16 thin films, allowing easy recovery, have been successfully prepared,[16-18] the activity of such

17 photocatalysts is considerably reduced, as the effective surface area is significantly decreased

18 during the preparation.[19] On the basis of practicality, immobilizing TiO_2 catalysts on to the surface

19 of magnetic nano- or microparticles has been a trend because they can be easily separated and

20 recovered from the solution with the help of an external magnet. By this method, to some degree,

21 the loss of catalysts can be avoided, less energy is required, and some required specifications of

22 applied materials can be obtained.[20-23] A number of materials with different elemental compositions

1 have been used as the magnetic core, such as Fe_3O_4, γFe_2O_3, $NiFe_2O_4$, $CoFe_2O_4$, $FeCo$, and Co_3O_4.

2 Among these materials, Fe_3O_4 has drawn a great attention due to its remarkable magnetic properties,

3 low toxicity, and biocompatibility.[24] The mesoporous TiO_2 shell in the composites is usually

4 prepared by sol–gel method to prevent Fe_3O_4 nanoparticles from being oxidized. However, after

5 introducing Fe_3O_4 as the cores of $Fe_3O_4@TiO_2$ hybrid nanostructures, photodissolution may occur

6 in the hybrid nanoparticles, which may decrease the photocatalytic efficiency of TiO_2 materials.[25]

7 Chemically inert surface of magnetic nanoparticles was provided by silica membranes, helping to

8 inhibit the oxidation of the Fe_3O_4 core by the holes photogenerated in outer TiO_2 layer.[26, 27]

9 However, the coating process of silicon membrane on the corn of Fe_3O_4 is complicated, the

10 synthesis of structure is unstable, and the superparamagnetic characteristic of the hybrid

11 nanoparticles significantly decreases. [28, 29] Up to now, considerable efforts have been devoted to

12 explore novel, versatile and magnetically-separable photocatalysts with core-shell

13 nanostructures.[28,29]

14   How to improve the photocatalytic activity of TiO_2 in visible region is another focus of recent

15 research on TiO_2 photocatalysis. Over the past decades, TiO_2 photocatalysts doped with metal or

16 metallic oxide, e.g., Pb, Au, Ag, Ag_2O, $AgPO_3$, $BiVO_4$, have been widely studied for improving

17 photocatalytic performance on the degradation of various organic pollutants under the irradiation of

18 visible light.[30-33] Here, metal nanoparticles act as a mediator in storing and shuttling photogenerated

19 electrons from TiO_2 surface to an acceptor.[20] A peculiar case of Ag was reported, where its

20 nanocomposite with TiO_2 can efficiently retard the e^--h^+ recombination because of the Schottky

21 barrier formed at the metale TiO_2 interface. The decrease of charge carriers recombination enhances

22 its photoactivity.[26] Furthermore, silver itself has been recognized as a natural antimicrobial agent

1   since ancient times, and silver can also act as an antimicrobial auxiliary agent as deposit on a TiO_2

2   surface.[19,34,35]

3   In the present paper, uniform sea urchin-like $Fe_3O_4@TiO_2$ nanocomposites, $Fe_3O_4@TiO_2$ NCs,

4   were successfully synthesized at 100% morphological yield by a modified hydrothermal method,

5   and sea urchin-like $Fe_3O_4@TiO_2@Ag$ nanocomposites, $Fe_3O_4@TiO_2@Ag$ NCs, were fabricated in

6    $AgNO_3$ solution under visible light by a photochemical reduction technique. $Fe_3O_4@TiO_2@Ag$ NCs

7   were prepared in order to possess the potential advantages: (i) easy recovery and multi-reuse ability;

8   (ii) excellent photocatalytic activities under visible irradiation; (iii) degradation and complete

9   mineralization for organics. The morphology, elemental composition, crystallinity and phase, pore

10   properties, and magnetic properties were studied by Transmission Electron Microscope (TEM),

11   field-emission scanning electron microscopy (FESEM), X-ray diffraction (XRD), (X-ray

12   photoelectron   spectroscopy   )XPS,   UV−vis   spectroscopy   (UV-vis-DR),   pore-size

13   distributions   ,andvibrating   sample   magnetometer(VSM).   The   catalytic   activities   of

14   $Fe_3O_4@TiO_2@Ag$ NCs were estimated by the catalytic reduction of Ampicillin under UV and

15   visible light. Furthermore, the intermediate products of the photocatalytic degradation of AMP at

16   different periods was investigated by high performance liquid chromatography-tandem mass

17   spectrometry (HPLC-MS) analysis, and the mineralization of AMP molecules was studied by TOC

18   analysis. And the multi-reuse property of $Fe_3O_4@TiO_2@Ag$ NCs was examined for the better

19   understanding of its potential capability for practical applications. Then, the photoinactivation

20   toward *E. coli*, *S. aureus* and *Asper. Niger* was carried out under visible-light irradiation.

21   **2. Experimental Section**

5

1   **2.1. Materials**

2   FeCl$_3$·6H$_2$O, sodium acetate, ethylene glycol, hydrochloric acid(36.5wt%), anhydrous ethanol,

3   ammonium hydroxide (NH$_3$·H$_2$O, 28wt %), sodium hydroxide, macrogol 4000-991, tetrabutyl

4   titanate (TBOT), silver nitrate (AgNO$_3$) were of analytical grade and purchased from Beijing

5   Chemical Reagent Company. Sodium ampicillin (AMP) was purchased from Sigma Aldrich (CAS:

6   69-52-3). Acetonitrile and methanol were of Chromatographic grade and bought from the TEDIA

7   Company, United States. Beef peptone, beef extract powder, yeast extract powder, glucose and agar

8   were of biochemical grade and purchased from Beijing AoBoXing Bio-Tech Co., Ltd. (China).

9   Ultrapure water (18 MΩ cm^{-1}) was used in all experiments.

10   **2.2．Synthesis of Fe$_3$O$_4$@TiO$_2$ microspheres (Fe$_3$O$_4$@TiO$_2$ MSs)**

11   As shown in Fig. 1 (a) step 1, Fe$_3$O$_4$ microspheres (Fe$_3$O$_4$ MSs) with an average size of 350 nm

12   were fabracated using the method introduced by C Liu.[36] Fe$_3$O$_4$@TiO$_2$ microspheres

13   (Fe$_3$O$_4$@TiO$_2$MSs) were prepared through a sol-gel process. The Fe$_3$O$_4$MSs were redisposed into a

14   mixture of ethanol (40 mL) and ammonium hydroxide (0.3 mL, 28 wt. %) under ultrasound for 20

15   min. Then the dispersion was transferred into a flask and heated at 45 °C under stirring. A mixture

16   of TBOT (0.8 mL)/ethanol (20 mL) was added into the suspension drop wise at a rate of 4 mL min^{-1},

17   and the sol gel process was allowed to proceed at 45 °C for 24 h. The resultant Fe$_3$O$_4$@TiO$_2$

18   core-shell microspheres were magnetically collected, washed with ultrapurewater and ethyl alcohol,

19   and dried at 40 °C for 12 h.

20   **2.3．Synthesis of sea urchin-like Fe$_3$O$_4$@TiO$_2$ nanocomposites (Fe$_3$O$_4$@TiO$_2$ NCs).**

1   As shown in Fig. 1 (a) step 2, $Fe_3O_4@TiO_2$ NCs were fabricated through a modified hydrothermal

2   method. The $Fe_3O_4@TiO_2$ core-shell microspheres were transferred into a Teflon-lined

3   stainless-steel autoclave (100 mL) containing 10 mL of 1.0 M NaOH solution, and the system was

4   hydrothermally treated. The powders were collected, washed with ultrapurewater and ethyl alcohol,

5   and dried at 40 °C for 12 h. Sea urchin-like corn-shell hollow $Fe_3O_4@$titanate nanocomposites

6   (Fe_3O_4/titanate NCs) were obtained. In order to prepare anatase TiO_2 crystal, sea urchin-like

7    $Fe_3O_4@$titanate hollow microspheres (0.1 g) were immersed in 10 mL 0.1 M HCl for 20 min,

8   washed with ultrapurewater water until neutral and then subsequently annealed under N_2 at a rate of

9   0.5 mL min^{-1} at 450 °C for 4 h to obtain $Fe_3O_4@TiO_2$ NCs.

10   **2.4. Synthesis of sea urchin-like $Fe_3O_4@TiO_2@Ag$ nanocomposites ($Fe_3O_4@TiO_2@Ag$ NCs).**

11   As shown in Fig. 1 (a) step 3, the $Fe_3O_4@TiO_2@Ag$ NCs were synthesized via a photoreduction

12   process under visible light. Initially, $Fe_3O_4@TiO_2$ NCs was added into 20 mL $AgNO_3$ aqueous

13   solution (Ag^+ mass concentration 20 mg L^{-1}); then, the mixtures were shaken for 30min in a

14   reciprocal shaker with agitation rate of 100 rpm under visible irradiation, obtained by three

15   multifilament lamps of 8 W with irradiation, at 25 °C. Agitation was provided by horizontal shaker.

16   After illumination, $Fe_3O_4@TiO_2@Ag$ NSs were collected, washed with ultrapure water and ethanol,

17   and finally dried in vacuum at 40 °C for 12 h.

18   **2. 5. Characterization**.

19   The morphology of the sample examined with a field emission scanning electron microscope

20   (FESEM JSM-7100F), high-resolution transmission electron microscope (TEM FEIF20) equipped

1 with an energy dispersive X-ray (EDX). The crystallinity and phase of $Fe_3O_4@TiO_2@Ag$ NSs was

2 determined by X-ray diffraction (XRD, D8 Advanced, Bruker). UV-Vis diffuse reflectance spectra

3 were conducted on a UV-Vis spectrophotometer (UV-3150, Shimadzu, Japan) attached with

4 integrating sphere. Barium sulfate ($BaSO_4$) pellets were used as reference to measure the visible

5 light absorption of $Fe_3O_4@TiO_2@Ag$ NSs. Nitrogen sorption isotherms were carried out at 77 K

6 using an Autosorb-1-C analyzer (USA Quantachrome Instruments), and the pore-size distributions

7 were derived from the adsorption branch of the isotherms using the BJH method. The magnetic

8 properties were measured with a vibrating sample magnetometer (VSM), Physical Property

9 Measurement System-9, at 25℃ as a function of the applied magnetic field between −12 and 12

10 kOe.

11 **2.6. Photocatalytic Experiments.**

12 The photocatalytic activities of the as-prepared Fe_3O_4 MSs, $Fe_3O_4@TiO_2$ NSs and

13 $Fe_3O_4@TiO_2@Ag$ NSs were evaluated by the degradation of AMP under ultraviolet and visible

14 irradiation. AMP is a common antibiotic used in human and animal medicine, and is an amphoteric,

15 beta-lactam of the penicillin class. [37] 0.02g of the sample was dispersed within a 20 mL AMP

16 solution with a concentration of 20ppm, which was stirred in the dark or light at 25℃ in the

17 process of reaction. Ultraviolet lamps (365 nm, 8 W) and visible lamps were used as the light

18 source, which was placed 10 cm away from the reaction vessel. The photocatalytic reaction was

19 started by turning on the lamp. All experiments were carried out at the natural pH of the solution

20 (~7) and the process was maintained at a constant temperature controlled by a thermoregulator. The

21 degradation of AMP was monitored by high performance liquid chromatography (HPLC) analysis

1   (Shimadzu, Japan) with a C_{18} (5 μm, 4.6 mm×150 mm) column. Acetic acid (1M), KH_2PO_4 buffer

2   solution (1 M), acetonitrile and ultrapure water (v/v/v/v=1:10:80:909) was used as mobile phase, at

3   a flow rate of 1mL·min^{-1}. The detector wavelength was set as 220nm and injection volume was

4   20μL. The degradation rate of AMP could be calculated using Eq. (1) shown below.

5    $$\text{Degradation rate (\%)}= \frac{C_0-C_t}{C_0} \times 100\% \qquad \text{Eq. (1)}$$

6   Where C_0 and C_t are the initial and final concentration (mgL^{-1}), respectively. The intermediate

7   products of the photocatalytic degradation of AMP by $Fe_3O_4@TiO_2@Ag$ NSs at different periods of

8   exposure to light were investigated by high performance liquid chromatography-tandem mass

9   spectrometry (LC-MS) analysis using acetonitrile/water as the eluent.

10   **2.7. Mineralization studies by TOC analysis.** The mineralization of $Fe_3O_4@TiO_2@Ag$ NSs for

11   AMP was studied by measuring the total organic carbon (TOC) contents of AMP solution after the

12   degradation with different time spans using a TOC analyzer (TOC-L CPH, Shimadzu, Kyoto,

13   Japan). The corresponded concentrations were also monitored for comparison by HPLC analysis at

14   the wavelength of 220 nm.

15   **2.8. Antibacterial Tests.** In general, suspensions (40 mL) of the as-prepared photocatalyst

16   nanoparticles (0.04 g) were uniformly dripped by ultrasonic dispersion onto filter papers (Φ5 mm)

17   separately. After being dried in air, the filter papers were then placed onto the bottom of a Petri dish

18   for antibacterial experiments. The characteristics of different Antibacterial Films are showed in

19   Table S3. Control samples were prepared using filter paper without loading any nanoparticles.

20   Antibacterial activities were evaluated using Gram-negative Escherichia coli (*E. coli*, ATCC 8099),

21   Gram-positive staphylococcus aureus (*S. aureus*, ATCC 6538), and a common mycosis-Candida

1 albicans (*Asper. Niger*, ATCC 16404). Before the microbiological experiments, all glasswares were

2 sterilized by autoclaving at 120 °C for 30 min. *E. coli* and *S. aureus* suspensions (0.2 mL, 10^4-10^5

3 CFU mL^{-1}) were spread on the surface of LB plates, and *Asper. Niger* suspensions (10^4-10^5 CFU

4 mL^{-1}) on the surface of YPD plates, then, antibacterial and blank films were placed on the plates.

5 The plates were incubated at 37 °C under visible light for 24 h. All tests were performed in triplicate,

6 and the results were averaged.

7 **3. Results and discussion**

8 **3.1. Controllable synthesis of Fe$_3$O$_4$@TiO$_2$@Ag NCs**

9 **3.1.1. Synthesis of Fe$_3$O$_4$@TiO$_2$@Ag NCs**
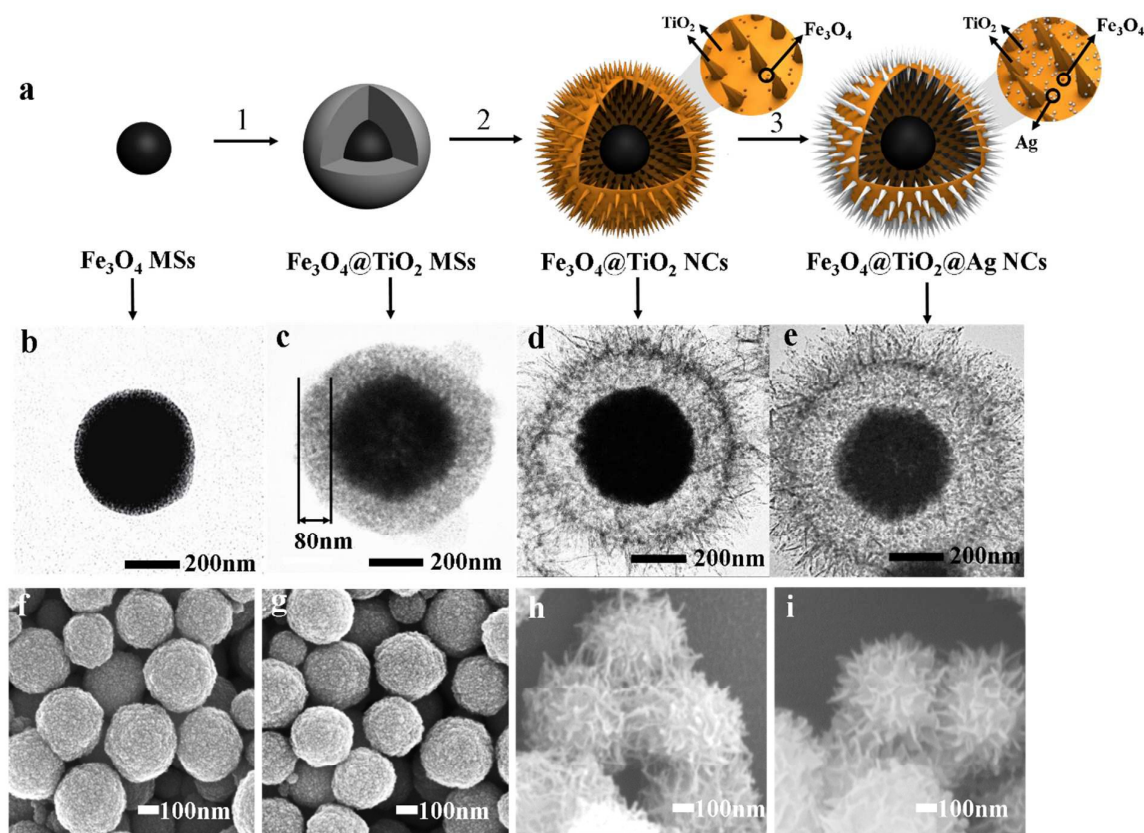
10

11 **Fig. 1** Formation of Fe$_3$O$_4$@TiO$_2$@Ag NCs. Proposed mechanism can be considered as three steps: (1) formation

12 of Fe$_3$O$_4$@TiO$_2$ core-shell microspheres; (2) formation of TiO$_2$ nanofiber and yolk-shell hollow shell; (3) coating

1   of Ag nanoparticals. a-d) TEM images of Fe_3O_4 MSs (a) Fe_3O_4@TiO_2 MSs (b), Fe_3O_4@TiO_2 NCs (c),

2   Fe_3O_4@TiO_2@Ag NCs (d); e-h) FESEM images of Fe_3O_4 MSs (e) Fe_3O_4@TiO_2 MSs (f) Fe_3O_4@TiO_2 NCs (g),

3   Fe_3O_4@TiO_2@Ag NCs(h)

4   Fig. 1 illustrates the diagrammatic sketch of the synthesis of Fe_3O_4@TiO_2@Ag NCs. (a), and

5   shows the corresponding TEM images (b-e) and FESEM images (f-i), different nanostructures. In

6   step (1), the diameter of Fe_3O_4 microspheres, Fe_3O_4 MSs, was approximately 350 nm as shown in

7   Fig. 1b, and the magnetic core ensures the easy separation of nanocomposites from reactant mixture.

8   A uniform interlayer of TiO_2 with a thickness of about 80 nm was coated onto Fe_3O_4 MSs through a

9   controlled sol-gel process to formationFe_3O_4@TiO_2 core-shell microspheres, Fe_3O_4@TiO_2 MSs as

10   in Fig. 1c.[36] Fe_3O_4 MSs and Fe_3O_4@TiO_2 MSs were monodispersed uniformly in size as in Fig. 1f,g.

11   In step (2), Fe_3O_4@TiO_2NCs with diameter of approximately 700nm was synthesized by a modified

12   hydrothermal method, and its shell consists of radically assembling nanofibers with average

13   diameter of 10 nm and average length of 100 nm as in Fig. 1d. The formation of radial nanofiber

14   structure can be explained as that, when the Fe_3O_4@TiO_2 MSs were immersed in alkaline solution,

15   the alkaline solution permeated into the inner cavity, which is benefited by the porous of the TiO_2

16   shell. Simultaneously, titanate appeared on the interface of the TiO_2 layer from the interaction

17   between the OH− ions and amorphous TiO_2.[38] As the reaction prolonged, the TiO_2 layer was etched

18   from its interior and exterior surfaces, and sodium titanate gradually generated on the surface of the

19   layer. Then the TiO_2 layer was exhausted and the outer cavity in situ appeared. As the sodium

20   titanate grew from short nanowires to long nanofibers, the sea urchin-like yolk-shell structure of

21   double shells was fabricated.[39] The process, that the tiny sodium titanate seeds were dissolved and

22   recrystallized into large and long sodium titanate nanofibers, can be attributed to Ostwald ripening.

1   [38-40,41] There was no damage on three dimensional structure during the formation of the structure of

2   both radial and uniform TiO_2 nanofibers and novel shells as in Fig. 1h.   In step (3), the structure of

3      $Fe_3O_4@TiO_2@Ag$ NCs with a Fe_3O_4 magnetic core and a shell of TiO_2 /Fe_3O_4/Ag

4   nanoheterojunctions nanofiber were formatted. The diameter of $Fe_3O_4@TiO_2@Ag$ NCs remained

5   approximately 700 nm, and the nanofibers on the surface became a little shorter and thicker after

6   coating with Ag nanopartical as in Fig. 1e. The surface appearance of $Fe_3O_4@TiO_2@Ag$ NCs

7   remained about the same with $Fe_3O_4@TiO_2$ NCs Fig. 1i.

8   **3.1.2. Influence of hydrothermal time on $Fe_3O_4@TiO_2@Ag$ NCs**
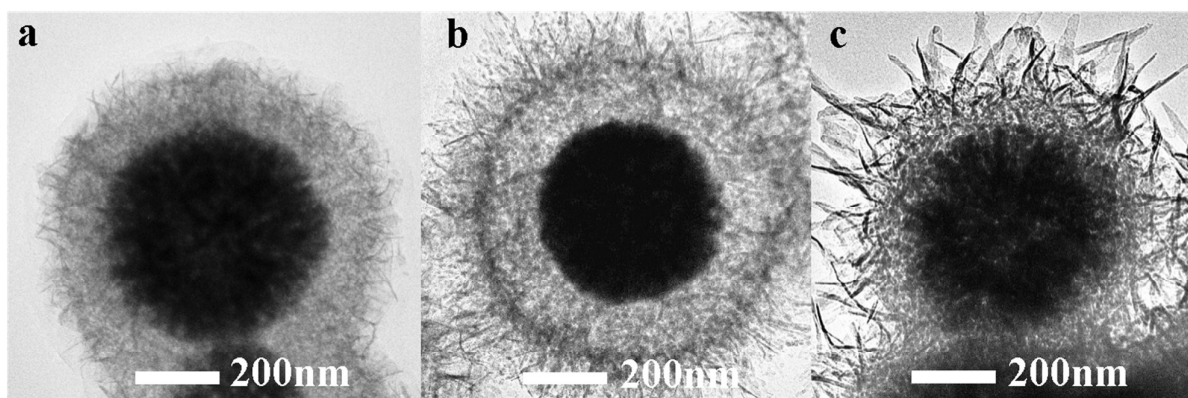
9

10   **Fig. 2** Effect of hydrothermal time on $Fe_3O_4@TiO_2@Ag$ NCs for 1h (a), 2h (b), 3h (c).

11   Hydrothermal time normally has a great effect on the morphology of nanomaterial. TEM

12   images of nanofibers and hollow shells with different structures were created by hydrothermally

13   treating the as-synthesized $Fe_3O_4@TiO_2$ MCs in a hydroxide solvent sodium at various

14   hydrothermal times as displayed in Fig. 2. The porosity of the nanocomposite was enhanced and the

15   hybrid shell on the microsphere was getting longer and thicker nanofibers, as the hydrothermal time

16   changed from1h, to 2h, to 3h under otherwise identical conditions. After 1 h reaction, short and thin

1   hybrid nanofibers were formed with about 50 nm in length and 2 nm in diameter as shown in Fig.

2   2a. More hybrid nanofibers grew to the size of approximately 100 nm in length and 10 nm in

3   diameter, and yolk–shell morphologies were observed after 2 h reaction as in Fig. 2b. Compared

4   with reported methods, for instance, a SiO_2 sandwich layer method,[27, 28] the presence of a hollow

5   provided a novel approach to inhibit the oxidation of the Fe_3O_4 core by the holes photogenerated in

6   the outer layer TiO_2. After 3 h reaction, the nanofibers in the outer shell still grew to possess an

7   average diameter of 20 nm and length of 150 nm, however, leaving the yolk–shell hollow

8   morphologies almost disappear as in Fig. 2c. The result was further confirmed in the FESEM

9   images as in Fig. S1, Supporting Information. It can be seen that the fiber-like nanocrystals on the

10   shells were formed after 1h; as the reaction continued, the crystallization extended into the internal

11   layer to yield a considerable amount of nanocrystals, and this was accompanied by the continuous

12   growth of the superficial nanofiber crystals.

13   It has been proved that the hydrothermal time not only promoted the crystal growth of the

14   surface, but also facilitated the formation of the homogenously structured porous shell. The

15   mesoporous hollow shell was created by hydrothermally treating the as-synthesized $Fe_3O_4@TiO_2$

16   MSs with NaOH as porosity modifier. The shells appeared to have different controllable pore

17   feature. Specific surface area and average pore size were measured by N_2 adsorption–desorption

18   experiments with the samples, and the results are shown in Table S1 (Supporting Information).

19   When the hydrothermal treating time was 1h, the abundant disordered micro-mesoporous were

20   observed on the shells of nanocomposites; more mesoscale porous-looking shells became

21   significant as the reaction time increased, which is good for the adsorption of organic contaminant

22   and heavy metal ion.[30] As the pore size of the $Fe_3O_4@TiO_2@Ag$ NSs increases along with the

1 growth of crystallite, there is a constant decrease in surface area. Considering the specific structure

2 after 2h hydrothermal treatment, it was selected for further studies.

3 **3.1.3. Influence of hydrothermal temperature on Fe₃O₄@TiO₂@Ag NCs**
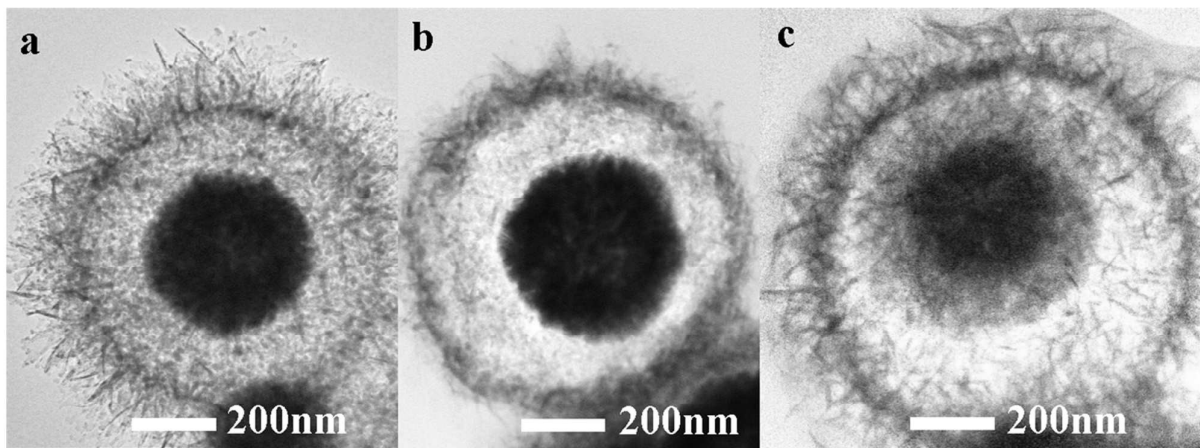
4

5 **Fig. 3**-Effect of hydrothermal temperature reaction 2 h for 120℃(a), 140℃(b), and 160℃(c).

6   In addition to hydrothermal time, hydrothermal temperature also had a great effect on the

7 structures of the $Fe_3O_4@TiO_2@Ag$ NCs, and TEM images were also displayed in Fig. 3. Different

8 volumes of hollow shells were fabricated by hydrothermally treating the as-synthesized

9 $Fe_3O_4@TiO_2$ MCs in a hydroxide solvent sodium at various hydrothermal temperatures. As the

10 reaction continued, the volume of nanospheres went up gradually due to the dramatic increase of the

11 hollow volume in TiO_2/Ag shells. The diameters of $Fe_3O_4@TiO_2@Ag$ NCs were respectively 700

12 nm, 905 nm, 1012 nm after hydrothermally treating at 120 °C, 140 °C and 160 °C. As can been see

13 from FESEM images, there are no significant difference on the surface morphology of

14 $Fe_3O_4@TiO_2@Ag$ NCs at various hydrothermally temperatures (Fig. S2). The nanostructures after

15 2h hydrothermal treating at 120°C was selected as photocatalysts in this study.

1   **3.2 Characterization**

2   **3.2.1 HRTEM and elemental mapping**

3   To confirm the distribution of Fe_3O_4@TiO_2@Ag NCs, samples were analyzed by EDX elemental

4   mapping as in Fig. 4. The different color areas, shown in Fig. 4b–e**,** indicate O–, Fe–, Ti–, and

5   Ag-enriched areas of the sample respectively. It showed that the well-dispersed of TiO_2 nanofiber of

6   the hollow cavities and Ag nanoparticles are loaded both on the nanofibers and inside the hollow

7   cavities, and the structure of Fe_3O_4@TiO_2@Ag NCs with a Fe_3O_4 magnetic core and a TiO_2

8   /Fe_3O_4/Ag nanoheterojunctions shell with hollow cavity were further conformed. In conclusion,

9   high-density TiO_2 and Ag NPs have been immobilized on the surface of Fe_3O_4 MSs and

10   Fe_3O_4@TiO_2 NCs, respectively. The content of Ag NPs in the Fe_3O_4@TiO_2@Ag NCs is 2.1wt. %.

11   The mesoporous characteristic and large surface area improved the effective contact area with Ag

12   nanoparticals, and the excellent photocatalytic properties of TiO_2 nanofiber and shell provided a

13   favorable environment for coating Ag both on the nanofibers and inside the hollow cavities as in Fig.

14   4e.While Fe_3O_4 on shell may come from the Fe_3O_4 magnetic core during modified hydrothermal

15   method, which was further confirmed by HRTEM image of Fe_3O_4@TiO_2 NCs and

16   Fe_3O_4@TiO_2@Ag NCs in Fig. 4f. After synthesis of Fe_3O_4@TiO_2 NCs, there were trace amount of

17   Fe_3O_4 nanoparticals modified on the TiO_2 nanofibers. Meanwhile, Ag nanoparticles were found in

18   size of about 4 nm uniformly in the HRTEM image of heterozygosis nanofiber. The interplanar

19   spacing of 0.352 nm corresponds to the [110] plane of TiO_2, the 0.256 nm corresponds to the [311]

20   plane of Fe_3O_4, while 0.226 nm correspond to the [111] plane of Ag in Fig. 4g. The pattern shows

21   rings that may be indexed to the [311] and [440] lattice planes of Fe_3O_4 (JCPDS File No.19-0629),

Nanoscale Accepted Manuscript

1   [101], [440], [105] plans of TiO_2 (JCPDS card No. 37-0951), and [111] plane of Ag (JCPDS card

2   no.04-0783). Electron mapping image were analyzed, the different color areas shown in parts h–j of

3   Fig. 4 indicate Fe–, Ti–, and Ag-enriched areas of the sample, respectively, which indicate the

4   coexistence of TiO_2 and Ag as well as Fe_3O_4 in the hollow cavities and heterozygosis nanofiber.
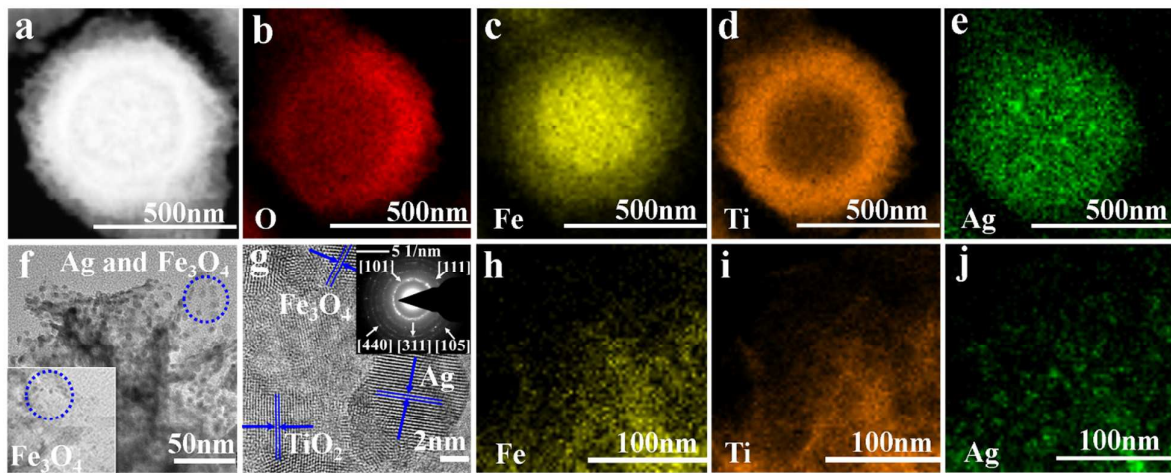
5

6   **Fig. 4** a) TEM image of $Fe_3O_4@TiO_2@Ag$ NCs; b–e) elemental mapping of the $Fe_3O_4@TiO_2@Ag$ NCs from the

7   TEM images based on O (b), Fe (c), Ti (d) and Ag (e); f) Nanofibers enlarged portion of $Fe_3O_4@TiO_2@Ag$ NCs,

8   the inset on the left is nanofibers of $Fe_3O_4@TiO_2$ NCs; g) HRTEM image of $TiO_2/Fe_3O_4/Ag$ heterojunction, the

9   inset on the right is the selected area electron diffraction (SAED) pattern. h–j) elemental mapping of the TiO_2

10 $/Fe_3O_4/Ag$ nanofiber from TEM images based on Fe (h), Ti (i) and Ag (j).

11   **3.2.2 Elemental compositions analysis with XRD and XPS**

12   To prove the successful synthesis of $Fe_3O_4@TiO_2@Ag$ heterozygosis, their elemental

13   compositions and chemical status were analyzed by XRD and XPS. The change of crystal structures

14   during the synthesis process of $Fe_3O_4@TiO_2@Ag$ NCs was studied by XRD as in Fig. 5a. Wide

15   angle XRD patterns show that the characteristic broad diffraction peaks correspond to the spinel

16   Fe_3O_4, titanate, anatase TiO_2 and cubic phase Ag NPs in the composite. The specific XRD of Fe_3O_4

1   is characterized by six peaks positioned at the 2θ values of 30.0°, 35.3°, 42.9°, 53.5°, 57.0° and

2   62.4°, which correspond to the [220], [311], [400], [422], [511], and [440] lattice planes of the cubic

3   phase of Fe_3O_4 (JCPDS card No. 19-0629), respectively. After hydrothermal treatment, the peaks at

4   2θ values of 24.38°, 29.95° and 47.86° correspond to the reflections from the [110], [-501], [-314]

5   planes and demonstrate the formation of the titanate phase (JCPDS card No. 37-0951), which

6   yielded from the reaction of TiO_2 with the alkaline solution. It is possible that some oligomeric

7   species of sodium titanate may be produced during NaOH etching.[4] Although sodium titanate has a

8   number of applications, its photocatalytic activity is considerably lower than that of anatase phase

9   titania, and therefore, it is not a desirable phase in our synthesis. After acid-treatment and

10   calcination, the patterns of the $Fe_3O_4@TiO_2$ NCs show several additional peaks compared with the

11   patterns of Fe_3O_4/titanate NCs, which can be attributed to the anatase phase of TiO_2, whose

12   photocatalytic activity is considerably high. The extra peaks located at 25.3°, 37.9°, 48.0° and

13   53.9°correspond to the reflections from the [101], [004], [200], and [105] planes of the anatase

14   phase (JCPDS card no. 21-1272). After loading the Ag NPs on the surface of the $Fe_3O_4@TiO_2$ MS,

15   several characteristic peaks are found at 2θ of 38°, 44°, 65° and77°, which are ascribed to the [111],

16   [200], [220] and [311] planes of face-centered cubic Ag phase (JCPDS card no.04-0783). These are

17   in agreement with the SAED patterns as shown in Fig. 4g. The characteristic XRD patterns of

18   $Fe_3O_4@TiO_2@Ag$ NCs imply that the current system is suitable for the synthesis of anatase phase.

19   Compared with $Fe_3O_4@TiO_2$ NCs, new peaks of Ag were found in $Fe_3O_4@TiO_2@Ag$ NCs in

20   addition to the Ti, O, and C elements based on XPS survey spectra shown in Fig. 5b, and the surface

21   concentration of C, O, Fe, Ti and Ag elements were 22.59 %, 56.62 %, 1.47 %, 18.22 %,1.11%

22   respectively. The samples contained Fe in Fig.5c, were confirmed by the binding energies of Fe

17

1   $2p_{3/2}$ and $2p_{1/2}$ at ~710 eV and ~724 eV, respectively. These binding energies can be assigned to

2   Fe_3O_4. Meanwhile, it showed the signals of Ti $2p_{3/2}$ and Ti $2p_{1/2}$ at ~458 eV and ~464 eV in Fig. 5d

3   respectively, corresponding to TiO_2. It can be observed that the surface concentration of O is

4   relatively high, due to TiO_2 coating. Metallic Ag loading can be confirmed by the presence of the

5   signals of Ag $3d_{5/2}$ and Ag $3d_{3/2}$ at 368.5 eV and 374.5 eV in Fe₃O₄@TiO₂@AgNCs as shown in Fig.

6   5e respectively.
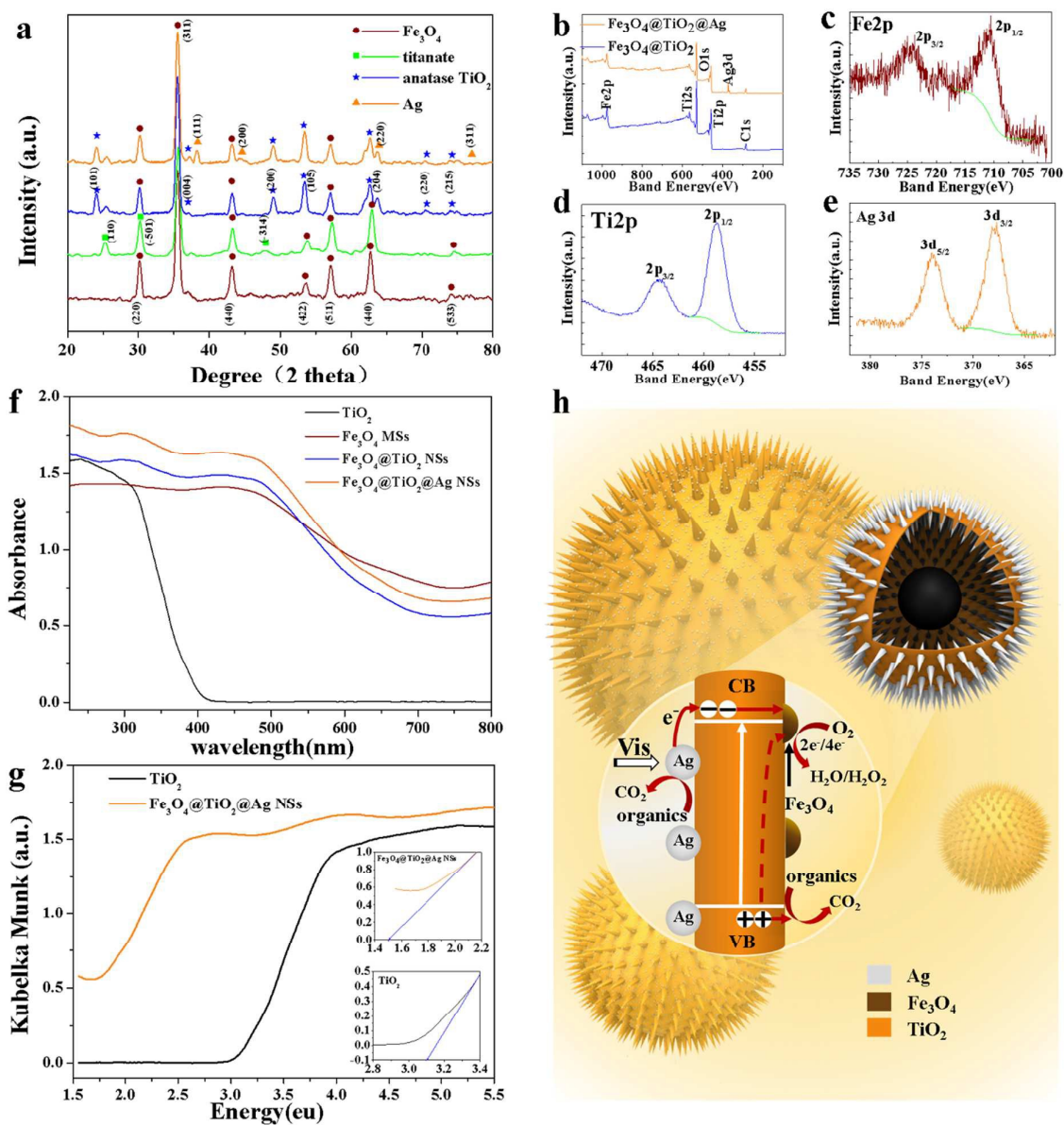
7

1   **Fig. 5** a) XRD patterns of Fe_3O_4 MSs, Fe_3O_4/titanate NSs, $Fe_3O_4@TiO_2$ NCs and $Fe_3O_4@TiO_2@Ag$ NCs; b)

2   Survey scan of $Fe_3O_4@TiO_2$ NCs and $Fe_3O_4@TiO_2@Ag$ NCs; c) Fe2p high-resolution XPS spectra; d) Survey

3   scan of Ti2p high-resolution XPS spectra;   e) Ag3d high-resolution XPS spectrum of $Fe_3O_4@TiO_2@Ag$ NCs; f)

4   UV-vis absorption spectra of TiO_2, Fe_3O_4 MSs, $Fe_3O_4@TiO_2$ NCs and $Fe_3O_4@TiO_2@Ag$ NCs; g) Kubelka-Munk

5   plot for the estimation of the band-gap energies of TiO_2 and $Fe_3O_4@TiO_2@Ag$ NCs; h) Schematic diagrams for

6   the possible photocatalytic mechanism of $Fe_3O_4@TiO_2@Ag$ NCs。

7   **3.2.3 UV-vis diffeactance reflectance spectra analysis**

8   The UV-vis diffuse reflectance spectra for TiO_2, Fe_3O_4 MSs, $Fe_3O_4@TiO_2$ NCs and

9     $Fe_3O_4@TiO_2@Ag$ NCs were showed in Fig. 5f**.** The $Fe_3O_4@TiO_2$ NCs and $Fe_3O_4@TiO_2@Ag$ NCs

10   photocatalyst presented an enhanced adsorption in the visible region from 400 to 600nm. Pure TiO_2

11   had a broad intense adsorption in the UV region below 400 nm. The band-gap energy was

12   calculated by the Kubelka-Munk (KM) method.[42] The band-gap energy value, *Eg.* was determined

13   using the theory of optical adsorption for allowed direct transitions as in Eq. (2).

14     $$\alpha hv = A(hv - Eg.)^{1/2} \qquad\qquad (2)$$

15   Where *A* is a constant relative to the material, *hv* is the discrete photon energy, and α is the

16   adsorption coefficient for the characterization of optical absorption edge energy and could be

17   calculated from the diffuse reflectance data using the KM method. The *Eg.* value can be obtained by

18   extrapolating a linear fit of $(\alpha hv)^2$ against *hv* to zero. It is observed that the band-gap energy of pure

19   TiO_2 is from 3.0eV to 3.2eV, while the $Fe_3O_4@TiO_2@Ag$ NCs presents even lower band energy

20   with the values of 1.5eV as shown in Fig. 5g. It has been reported by Kamat,[43] that the electrons

21   can be transferred from the excited TiO_2 to the metallic nanoparticles that work as co-catalysts until

22   the two systems attain an equilibrium. When Fe_3O_4 cocatalyst and Ag nanoparticles are

1   simultaneously deposited on the surface of $Fe_3O_4@TiO_2@Ag$ NCs, it is clearly found that the

2   photocatalytic performance of resulting $TiO_2/Fe_3O_4/Ag$ heterojunction has been further improved,

3   which can be well explained by the synergistic effect of Fe (III) and Ag nanoparticles.[44,45] The

4   loading of Ag nanoparticles leads to the production of more photogenerated charges in

5    $TiO_2/Fe_3O_4/Ag$ heterojunction via LSPR absorption of Ag nanoparticles, and enhances band-gap

6   absorption of TiO_2, while the Fe(III) cocatalyst provides as active sites for oxygen reduction by the

7   effective transfer of photogenerated electrons to oxygen(Fig.5h).[44-46] The electron accumulation

8   increases the Fermi level of the heterojunction to more negative potentials; the resultant Fermi level

9   of the composite shifts closer to the conduction band of the semiconductor. Therefore the involved

10   edge energy Eg. in the electron transfer from TiO_2 to the heterojunction is lower than bare TiO_2,

11   which provide strong visible-light sensitization. As a result, enhanced photocatalytic activity is

12   realized in $Fe_3O_4@TiO_2@Ag$ NCs.

13   **3.2.4 N_2 adsorption/desorption isotherms**

14
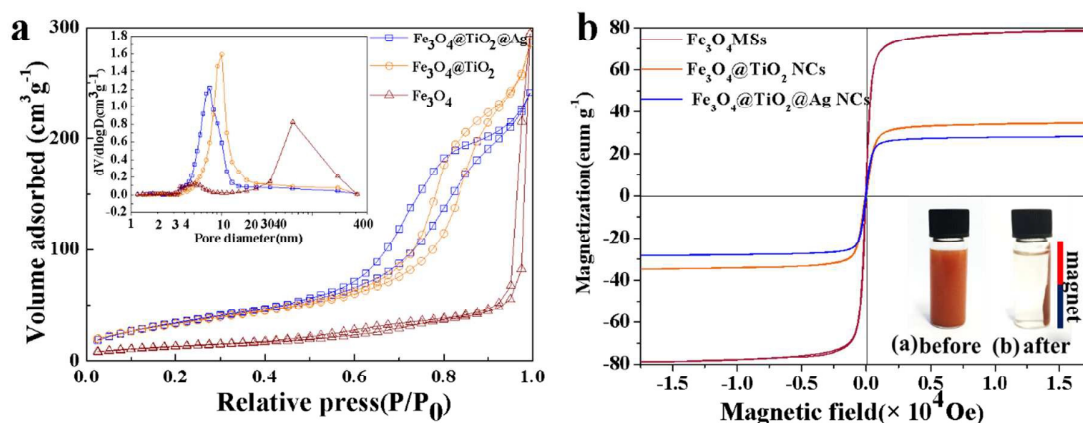
15   **Fig. 6** a) Nitrogen adsorption-desorption isotherms and the corresponding Barrett–Joyner–Halenda (BJH) pore

1   diameter distribution curve (inset) of Fe_3O_4 MSs, Fe_3O_4@TiO_2 NCs and Fe_3O_4@TiO_2@Ag NCs; b)

2   Magnetization curves of the Fe_3O_4 MSs, Fe_3O_4@TiO_2 NCs and Fe_3O_4@TiO_2@Ag NCs, respectively. The inset is

3   a photograph before and after magnetic separation.

4

5   Fig. 6a exhibits the N_2 adsorption/desorption isotherms and pore diameter distribution curves

6   of Fe_3O_4 MSs, Fe_3O_4@TiO_2NCs and Fe_3O_4@TiO_2@AgNCs. The isotherms of Fe_3O_4 are type III ,

7   showing little or no pore on the Fe_3O_4 surface morphology. The average pore diameter obtained via

8   the BJH method from the adsorption branch is 4.733 nm. The surface area and the total pore volume

9   are 46.039 m^2 g^{-1} and 0.4571 cm^3 g^{-1}. The isotherms of Fe_3O_4@TiO_2NCs and

10   Fe_3O_4@TiO_2@AgNCs are type-IV with H_2 hysteresis loops, suggesting mesoporous characteristic.

11   The average pore diameter obtained via the BJH method from the adsorption branch is 9.057 nm,

12   the surface area and the total pore volume are 125.349 m^2 g^{-1} and 0.4434 cm^3 g^{-1}, respectively.

13   After coating with Ag nanoparticles, the surface area is increased to 131.175 m^2 g^{-1}, while the

14   average pore diameter and total pore volume decrease to 6.821nm and 0.399cm^3 g^{-1} respectively.

15   **2.2.5 Magnetic behavior**

16   Fig. 6b shows the magnetic hysteresis loops of Fe_3O_4MSs, Fe_3O_4@TiO_2NCs and

17   Fe_3O_4@TiO_2@AgNCs at room temperature. As can be seen, they exhibit superparamagnetic

18   behavior, little hysteresis, remanence and coercivity, as the particles were composed of ultrafine

19   magnetite nanocrystals. The magnetization of Fe_3O_4 MSs, Fe_3O_4@TiO_2NCs and

20   Fe_3O_4@TiO_2@AgNCs is about 40.1 emu·g^{-1}, 34.5 and 26.5 emu·g^{-1}, respectively. The decrease in

21   magnetization is mainly due to the density decrease of Fe_3O_4 in the obtained composites after being

1   coated with TiO_2 and Ag. However, the $Fe_3O_4@TiO_2@Ag$ NCs still show strong magnetization,

2   which suggests their suitability for magnetic separation. The superparamagnetic characteristic and

3   high magnetization facilitate catalyst recovery from catalytic system via an external magnetic field

4   as in Fig.5b inset.

5   **3.3 Photocatalytic Activities**

6   **3.3.1 Photocatalytic degradation of AMP**
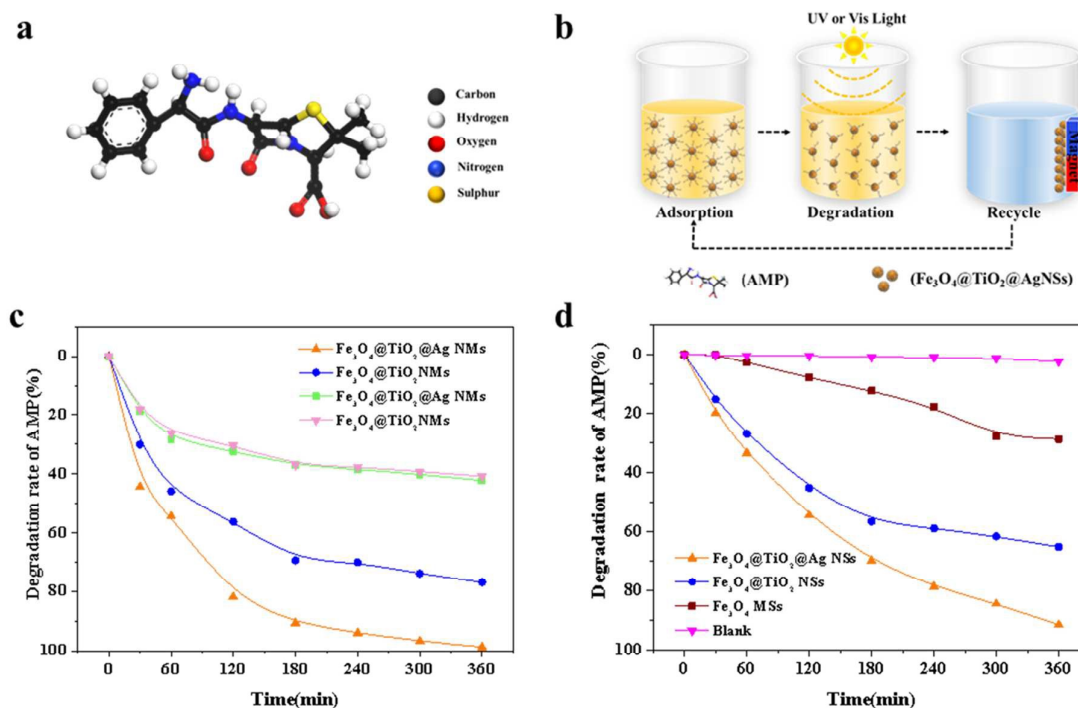
7

8   **Fig. 7** a) The ball-and-stick mode of AMP; b) Schematic illustration of the adsorption, degradation and recyclable

9   process of $Fe_3O_4@TiO_2@Ag$ NSs; c) Adsorption of AMP in dark and photocatalytic degradation of AMP under

10   UV light; d) Photocatalytic degradation of AMP under visible light. $[AMP]0 = 20$ mg L^{-1} and [Photocatalysts] = 1

11   mg L^{-1}.

12   As a common penicillin-class veterinary and human antibiotic, ampicillin (AMP) was chosen as the

13   model organic pollutant because antibiotic contaminants, as bio-refractory organics, show the

1   adverse effects on human, animal, and indigenous microbial communities as in Fig. 7a.[43]

2   Photocatalytic performances of Fe_3O_4 NSs, $Fe_3O_4@TiO_2$ NCs and $Fe_3O_4@TiO_2@Ag$ NCs were

3   comparatively evaluated by measuring the degradation of AMP aqueous solution under ultraviolet

4   and visible irradiation. Fig. 7b shows the schematic illustration of the adsorption, degradation and

5   recyclable process of $Fe_3O_4@TiO_2@Ag$ NCs. It can be seen that the degradation rates increase with

6   the increase of irradiation time for all samples as in Fig. 7c, d.

7   As showed in Fig. 7c**,** it is clearly observed that the $Fe_3O_4@TiO_2$ NSs displays a good

8   photocatalytic effect, and the decoration of $Fe_3O_4@TiO_2$ NCs with Ag nanoparticles is an effective

9   way to achieve higher catalytic efficiency, since the Ag loaded samples show higher photcatalytic

10   activity than that with $Fe_3O_4@TiO_2$ NCs only. After 180min of ultraviolet irradiation, the

11   degradation rates reach 90.6% for $Fe_3O_4@TiO_2@Ag$ NSs, while 69.4% for $Fe_3O_4@TiO_2$ NCs; and

12   after 360min, the degradation rates reach 98.7% for the $Fe_3O_4@TiO_2@Ag$ NCs, while 77.0% for

13    $Fe_3O_4@TiO_2$ NCs. The dependences of adsorption rates with time in dark are also revealed in Fig.

14   6c**,** they all reach the absorption equilibrium after 180min**,** which further confirms that there is no

15   significant difference of mesoporous characteristic between $Fe_3O_4@TiO_2$ NCs and

16    $Fe_3O_4@TiO_2@Ag$ NCs

17   Fig. 7d shows the photocatalytic activity of different catalysts evaluated by the degradation of

18   AMP under visible light irradiation. The relative photocatalytic activity of the catalysts for AMP

19   degradation follows the order: $Fe_3O_4@TiO_2@Ag$ NCs > $Fe_3O_4@TiO_2$ NCs > Fe_3O_4 MSs. In the

20   absence of catalysts, there was a slight photodegradation of AMP. Under 360min visible light

21   irradiation, the degradation rate of $Fe_3O_4@TiO_2@Ag$ NCs is above 91.5%, while that of

22    $Fe_3O_4@TiO_2$ MCs is 78%, and 29% the Fe_3O_4 MSs. The results indicate that $Fe_3O_4@TiO_2@Ag$

1   NCs has a better photocatalytic activity under visible light for the decomposition of AMP. The

2   higher activity is due to the enhanced photocatalytic activity as analyzed before. The observed

3   photocatalytic performance is better than that of most reported nanostructures, especially for visible

4   photocatalytic activity, which has been summarized in Table 1.

5

6

_____

Table 1. Performance of Photocatalytic Activity in Literature

Catalyst used and amount	Conc. and volume	Light	Time(min)	Degradation%	BET(m^2 g^{-1})	Magnetic properties(emu	Reference
Fe₃O₄@TiO₂@Ag (1mg mL⁻¹) $Fe_3O_4@TiO_2@Ag$ (1mg mL^{-1})	20mg L^{-1}	8W*3,	180(UV)	90.7(UV)	131.175	19.376	our work
	AMP	UV/Vis	360(Vis)	92.1(Vis)			
$Fe_3O_4@TiO_2@Au$ (50mg)	2.0 *10^{-5}M, 150mL	500W	50	100	50-60	26.5	47
	R6G	UV					
Ag_2O/TiO_2 (40mg)	10^{-5}M,40mL	40W	15,30	93,100	57.9	_____	48
	MO	UV					
Cyclodextrin-$Fe_3O_4@TiO_2$ (1 mg mL⁻¹)	20 mg L^{-1}	Hg Light	180	95	_____	28	49
	BPA	UV					
$Fe_3O_4@rGO@TiO_2$ (1.5g L⁻¹)	10 mg L^{-1}	300 W	150	~90	_____	34.202	50
	MB	UV					

2.3.2 Photocatalytic degradation products analysis

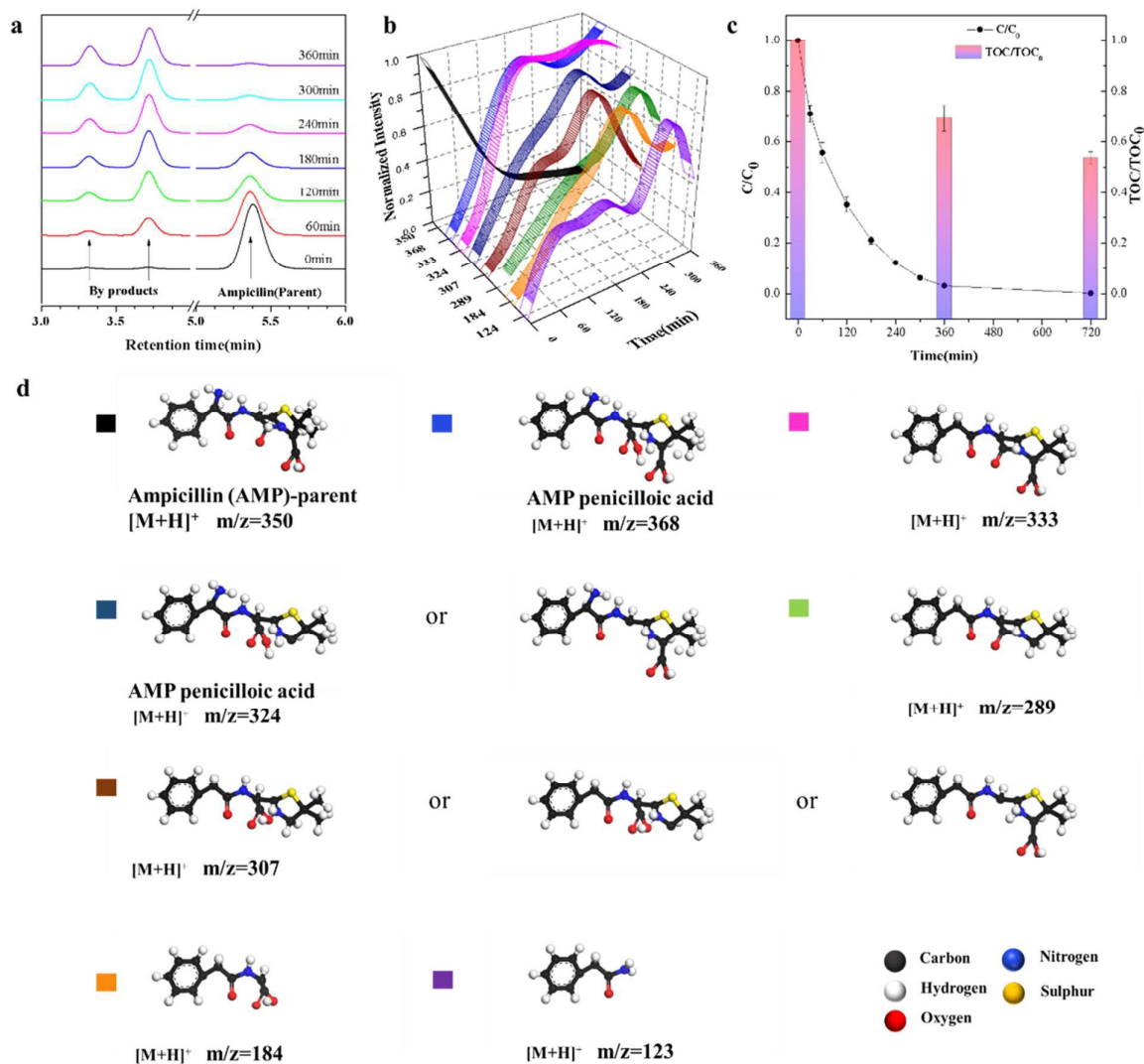**Fig. 8**. Photocatalytic degradation of Ampicillin by Fe_3O_4@TiO_2@Ag NCs. a) LC-MS chromatograms for different visible irradiation times at the pH of 7. Ampicillin and byproducts with different retention times are also indicated; b) Evolution of photodegradation products of Ampicillin *vs* irradiation time; c) TOC and concentration changes of APM solution along different treatment times. [AMP] $0 = 20$ mg L^{-1} and [Photocatalysts] $= 1$ mg L^{-1}. d) The molecular species corresponding to the different m/z ions.

The intermediate products of AMP photocatalytic degradation by $Fe_3O_4@TiO_2@Ag$ NCs at different periods of exposure to light were investigated by LC-MS analysis with methanol/water as the eluent. The chromatograms for the degradation of AMP within seven different UV exposure times are shown in Fig**.** 8a. The products at different retention times were mass-analyzed in the positive ion mode, and their evolutions with irradiation time are displayed in Fig. 8b. The seven main product ions depicted in the degradation of AMP are *m/z* 368, 333, 324, 307, 289, 184 and 124. The Ampicillin parent (*m/z*=350, retention time=5.3 min) observed in the chromatograms at short exposure times is identified. After 300 min of UV exposure, this cannot be observed any more in the chromatograms. Ions with molecular weights of *m/z* 368 and 333 observed in Fig. 7b recorded after 60 min irradiation suggest that the first step in the photocatalytic degradation is the reaction of hydroxyl radicals with the side chain C-N bond of AMP. It have been illustrated that there are two potential pathways for the formation of AMP byproducts observed in solutions mixed with $Fe_3O_4@TiO_2@Ag$ NCs (pH=7). Path 1 starts with the formation of penicilloic acid, is followed by decarboxylation, possibly via the attachment of primary COO^- group or carboxylic acid moiety formed by opening beta-lactam ring. Path 2 begins with the de-ammonification of parent AMP, yielding a byproduct of *m/z* = 333. Subsequent decarboxylation (*m/z* = 289), followed by hydrolysis, would also yield the species of *m/z* = 307. [44] It has been further discovered in our study that the amount of byproduct *m/z* = 123, increases significantly after 4 h photocatalytic degradation.

Antibiotic concentration decrease cannot reflect the mineralization extent of organic species because of the formation of some intermediates during the photocatalytic degradation process, which could also result in the decrease of antibiotic concentration. The mineralization effects of $Fe_3O_4@TiO_2@Ag$ NCs for AMP were further studied by recording the TOC contents of AMP

solution as well as the mass concentration at different times as in Fig. 7c. After treatment with

$Fe_3O_4@TiO_2@Ag$ NCs for 720 min, AMP concentration decreased about 99%, while TOC removal

rate was less than 46%, which indicates that complete mineralization was a relatively slow process

compared with the degradation of AMP molecules. So, longer treatment time would be required to

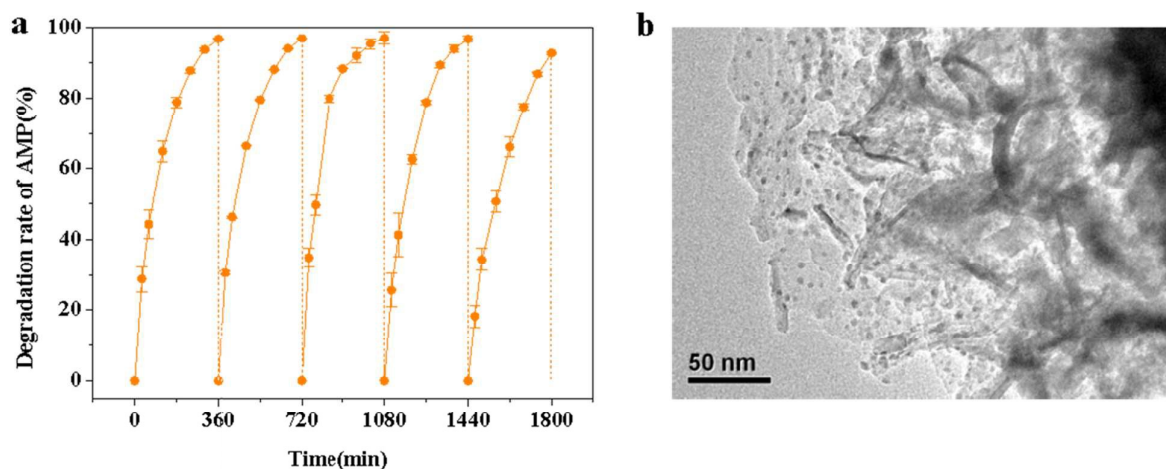obtain proper TOC removal efficiency.

3.3.3 Recycled performances

Fig. 9 a) Efficiency variation of the $Fe_3O_4@TiO_2@Ag$ NCs for the photocatalytic degradation of Ampicillin with

cycling under UV light. [AMP] ^{0} = 20 mg L^{-1} and [Photocatalysts] = 1 mg L^{-1}; b) HRTEM image of

$Fe_3O_4@TiO_2@Ag$ NCs after six cycles

Important considerations for the application of photocatalytic nanomaterials in water

remediation are their separation and reusability. The photocatalytic efficiency of the

$Fe_3O_4@TiO_2@Ag$ NCs for multiple usages was investigated. The $Fe_3O_4@TiO_2@Ag$ NCs, which

were magnetically separated from the dispersion after the photocatalytic degradation of AMP, were

reused for the photodegradation of a freshly prepared AMP solution as in Fig. 7b. As mentioned

earlier in the experiments, the AMP concentrations were determined by liquid chromatography and the visible exposure time was 360 min. The Fe$_3$O$_4$@TiO$_2$@Ag NCs were again magnetically separated and the experiments repeated. The results of photodegradation studies are shown in Fig. 9a. It can be seen that the efficiency of the Fe$_3$O$_4$@TiO$_2$@AgNCs for the photocatalytic degradation of AMP still maintains 95% efficiency, even after 5 cycles. The HRTEM image of the Fe$_3$O$_4$@TiO$_2$@Ag NCs, which had been used for five times shown in Fig. 9b, also proves the stability of synthesized catalysts.

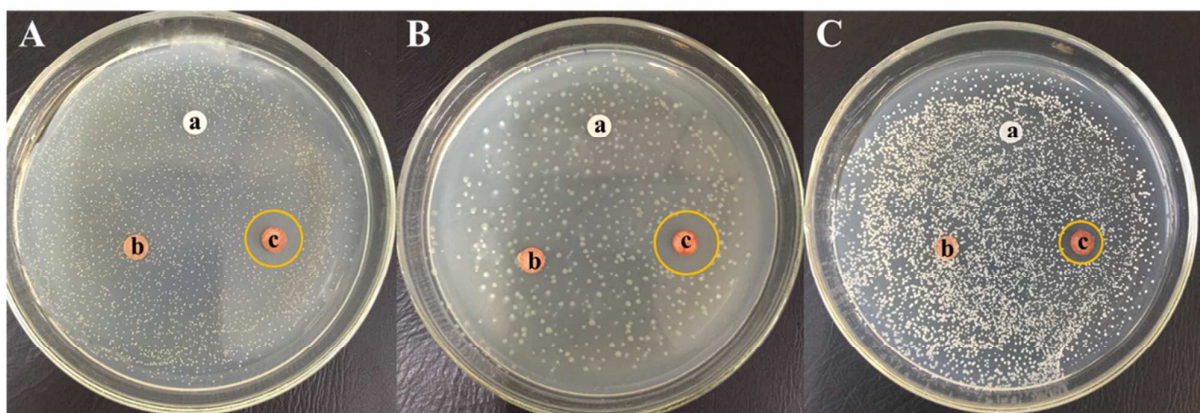### 3.4 Photocatalytic Antibacterial Characteristics

Fig. 10 Photographs of antibacterial results on *S. aureus* (A) *E. coli* (B) and *Asper. Niger*(C) for blank controller (a), Fe$_3$O$_4$@TiO$_2$ NCs films (b), and Fe$_3$O$_4$@TiO$_2$@Ag NCs films (c)

As showed in Fig. 10, the antimicrobial activity of Fe$_3$O$_4$@TiO$_2$@Ag NCs was assessed by the diameter of inhibition zone (DIZ) test with *S. aureus* (G$^+$), *E. coli* (G$^-$) and *Asper. Niger* (pathomycete) as the representative microorganisms. Robust growth of *S. aureus*, *E. coli* and *Asper. Niger* was vividly observed in control experiments. The *S. aureus*, *E. coli* and *Asper. Niger*, approximately 10^4 CFU mL^{-1}, were spread on the surface of an LB or YPD plate. Same as the control, Fe$_3$O$_4$@TiO$_2$ NCs and filter paper had no considerable antibacterial activity under visible

light, indicating that these material are not toxic to the microorganisms. Under visible light, $Fe_3O_4@TiO_2$ NCs did not show antimicrobial activities because TiO_2 could not be activated by visible light.[35] Unlike the former case, the $Fe_3O_4@TiO_2@Ag$ NCs showed a palpable DIZ value, indicating significant antibacterial activity against *S. aureus*, *E. coli* and *Asper. Niger*. The average DIZ values for *S. aureus* and *Asper. Niger* are 14 mm and 10 nm respectively, while the corresponding value for *E. coli* is merely 20 mm. It suggests that $Fe_3O_4@TiO_2@Ag$ NCs have more effective contact biocidal property for *E. coli*. It can be hence predicated that excellent biocidal function of $Fe_3O_4@TiO_2@Ag$ NCs is derived from Ag species and oxidative stress caused by photo-generated reactive radicals.[35]

3. Conclusion

In summary, the sea urchin-like $Fe_3O_4@TiO_2@Ag$ nanocomposites were successfully fabricated by controllable synthesis. It has been illustrated that a Fe_3O_4 core and a nanofiber shell of TiO_2/Ag nanoheterojunctions exist in sea urchin-like yolk-shell $Fe_3O_4@TiO_2@Ag$ nanocomposites. These nanocomposites possess tunable cavity size, adjustable shell layers with various morphologies nanofibers, high structural stability and large specific surface area. The Ag nanoparticles of approximately 1 nm in diameter were loaded both on the TiO_2 nanofibers and inside the cavities of sea urchin-like $Fe_3O_4@TiO_2$ nanocomposites uniformly. Furthermore, the Fe_3O_4 magnetic core facilitates the convenient recovery of the catalyst by applying an external magnetic field. Sea urchin-like $Fe_3O_4@TiO_2@Ag$ NCs displays excellent activities under UV and visible light and recycling properties in the catalytic reduction of organic molecules, such as Ampicillin, and it presents excellent broad-spectrum antibiosis under visible-light irradiation. It can be expected that the modified hydrothermal strategy combine with a calcination strategy provides a

very powerful method for controlling the morphology and porosity of sea urchin-like

$Fe_3O_4@TiO_2@Ag$ nanocomposites and for improving photocatalytic activity. Moreover, it should

be point that the platform can decorate a variety of heavy metal nanoparticles material has certain

novelty.

Supporting Information

Supporting Information is available from the Wiley Online Library or from the author.

References

1 A. Fujishima, K. Honda, *Nature*1972, **238**, 37; M. A. Fox ,M. T. Dulay,*Chem. Rev.* 1993,**93**, 341;

  A. Fujishima, X. T. Zhang, D. A. Tryk, *Surf. Sci. Rep.* 2008, **63**, 515.

2 J. Tian, Z. H. Zhao, A. Kumar, R. I. Boughtonc, H. Liu, *Chem. Soc. Rev*., 2014, **43**, 6920.

3. J. Tang, Z. Huo, S. Brittman, H. Gao, P. Yang, *Nat. Nanotechnol.* 2011, **6**, 568; W. Zhou, T. Li,

  J.Wang, Y. Qu, K. Pan, Y. Xie, G. Tian, L. Wang, Z. Ren, B. Jiang, H. Fu, *Nano Res.* 2014, **7**, 731;

  W. J. Ong, L. L. Tan, S. P. Chai, S. T. Yong, A. R. Mohamed, *NanoRes.* 2014, **7**, 1528.

4 J. B. Joo, Q. Zhang, I. Lee, M. Dahl, F. Zaera, Y. Yin, *Adv. Funct. Mater*.2012, **22(1)**, 166.

5 K. Maeda, K. Domen, *J. Phys. Chem. Lett.* 2007, **111(22)**, 7851.

6 J. B. Joo, I. Lee, M. Dahl, G. D. Moon, F. Zaera, Y.D. Yin, *Adv. Funct. Mater.* 2013, **23**, 4246.

7 X. H. Xia, D. L. Chao, X. Y. Qi, Q.Q Xiong, Y. Q. Zhang, J. P. Tu, H. Zhang, H. J. Fan, *Nano Lett.*

2013, **13(9)**, 4562.

8 Y. Dou, S.T. Zhang, T. Pan, S. Xu, A. Zhou, M. Pu, H. Yan, J.B. Han, M.Wei, D. G. Evans, X.

Duan,*Adv. Funct. Mater*. 2015, **25**, 2243.

9 J. H. Pan, X. Z. Wang, Q. Z. Huang, C. Shen, Z. Y. Koh, Q. Wang, A. Engel*, D. W.

Bahnemann,*Adv.Funct. Mater.* 2014, **24**, 95.

10 G. R. Meseck, R. Kontic, G. R. Patzke, S. Seeger, *Adv. Funct. Mater*.2012, **22**, 4433.

11 Z. H. Xu, M. Quintanilla, F. Vetrone, A. O. Govorov,M. Chaker, D. L. Ma.*Adv. Funct. Mater*.

2015, **25**, 2950.

12 C. Wang, L. Yin, L. Zhang, Y. Qi, N. Lun, N. Liu, *Langmuir* 2010, **26**, 12841.

13 Y. Ding, L. Zhou, L. Mo, L. Jiang, L. H. Hu, Z. Q. Li, S. H. Chen, S. Y. Dai, *Adv. Funct. Mater.*

2015, **25**, 5946.

14 W. F. Ma, Y. Zhang, L. L. Li, L.J. You, P. Zhang, Y.T. Zhang, J.M. Li, M. Yu, J. Guo, H.J. Lu, C.

C. Wang, *ACS Nano* 2012, **6(4)**, 3179.

15 J. W. Su, Y. X. Zhang, S. C. Xu, S. Wang, H. L. Ding, S. S Pan, G. Z Wang, G. H Li and H. J.

Zhao, *Nanoscale* 2014, **6**, 5181.

16 L. X. Yang, S. L. Luo, Y. Li, Y. Xiao, Q. Kang, Q. Y. Cai, *Environ. Sci. Technol.* 2010, **44(19)**,

7641.

17 P. Sangpour, F. Hashemi, A. Z. Moshfegh, *J. Phys. Chem. C* 2010, **114 (33)**, 13955.

18 L. Pan, X. D. Zhu, X. M. Xie, Y. T.Liu, *Adv. Funct. Mater.* 2015, **25**, 3341.

19 J. B. Joo, I. Lee, M. Dahl, G. D. Moon, F. Zaera, Y. D Yin, *Adv. Funct. Mater*. 2013, **23**, 4246.

20 R. Chalasani, S. Vasudevan, *ACS Nano* 2013, **7(5)**,4093.

21 W. W. Tang, G. M. Zeng, J. L. Gong, J. Liang, P. Xu, C. Zhang, B. B. Huang, *Sci. Total. Environ.* 2014, **468**,1014

22 H. Li, X. Z. Shi, L. Z. Qiao, X. Lu, G. W. Xu, *J. Chromatogr. A* 2013, **1275**, 9.

23 X. X. Ge, W. Y. Zhang, Y. H. Lin, D. Du, *Biosens. Bioelectron.* 2013, **50**, 486.

24 J. H. Gao, H.W. Gu, B. Xu, *Acc. Chem. Res.* 2009, **42(8)**, 1097.

25 H. R. Dong, G. M. Zeng, L. Tang, C. Z. Fan, C. Zhang, X. X. He, Y. He, *Water Res.* 2015, **79,** 128.

26 P. P. Qiu, W. Li, B. Thokchom, B. Park, M. C. Cui, D.Y. Zhao, J. Khim, *J. Mater. Chem. A* 2015, **3**, 6492.

27 C. X. Wang, L.W. Yin, L. Y. Zhang, L. Kang, X. F. Wang , R. Gao, *J. Phys. Chem. C* 2009, **113(10)**, 4008.

28 J. Li, L. Tan, G. Wang, M. Yang, *Nanotechnology* 2015, **26(9)**,095601.

29 J. W. Liu, J. J. Xu, R. C. Che, H. J. Chen, M. M. Liu, Z. W. Liu, *Chem-Eur. J.* 2013, **19(21)**, 6746.

30 R. Su, R. Tiruvalam, Q. He, N. Dimitratos, L. Kesavan, C. Hammond, J. A. L.-Sanchez, R. Bechstein, C. J. Kiely, G. J. Hutchings, F. Besenbacher, *ACS nano* 2012, **6(7)**,6284.

31 M. Miljevic, B. Geiseler, T. Bergfeldt, P. Bockstaller, L. Fruk, *Adv. Funct. Mater.*2014, **24**, 907.

32 X. Q. Zhang, Y. H. Zhu, X. L. Yang, Y. Zhou, Y. F. Yao, C. Z. Li, *Nanoscale*, 2014, **6(11)**,5971.

33 J. W. Xu, Z. D. Gao, K. Han, Y. M. Liu, Y. Y. Song, *ACS Appl. Mater. Interfaces* 2014, **6(17)**, 15122.

34 H. F. Li, H. T Yu, X. Quan, S. Chen, H. Zhao, *Adv. Funct. Mater*. 2015, **25**, 3074.

35 G. Xiao, X. Zhang, W. Y. Zhang, S. Zhang, H. J. Su, *Appl. Catal. B-Environ* 2015, **170**, 255.

36 C. X. Liu, Y. Y. Ji, T. W. Tan, *J. Alloy. Compd*. 2013, **570**, 23.

37 J. W. Peterson, L. J. Petrasky, M. D. Seymour, R. S. Burkhart., A. B. Schuiling, *Chemosphere*

2012, **87(8)**, 911.

38 Y. F. Tang, L. Yang, J. Z. Chen, Z. Qiu, Langmuir 2010, 26,10111.

39 H. J. Li, Y. Zhou, W. G. Tu, J. H. Ye, Z. G. Zou, *Adv. Funct. Mater.* 2015, **25**, 998.

40 P Wang, D Chen, F Q Tang, *Langmuir*, 2006, **22(10)**, 4832.

41 J. W. Liu, J. J. Xu, R. C. Che, H. J. Chen, Z. W. Liu, F. Xia, *J. Mater. Chem.* 2012, **22**, 9277

42 S.K. Kansal, M. Singh, D. Sud, *J. Hazard. Mater.*2007, **141**, 581.

43 P.V. Kamat, Photophysical, Photochemical and photocatalytic aspects of metal nanoparticles, J.

Phys. Chem. B 106 (2002) 7729–7744.44H. G. Yu, G. Q. Cao, F. Chen, X. F. Wang, J. G. Yu, M.

Lei, *Appl. Catal. B-Environ* 2014, **160**, 658.

45 H. G. Yu, L.L. Xu, P. Wang, X. F. Wang, J. G. Yu, *Appl. Catal. B-Environ* 2014, **144**, 75.

46. H. Wei, E Wang, *Chem. Soc. Rev.* 2013, **42(14)**, 6060.47 X. Q. Zhang, Y. H. Zhu, X. L. Yang, Y.

Zhou, Y. F. Yao, C. Z. Li, *Nanoscale* 2014, **6**, 5971.

47 X. Q. Zhang, Y. H. Zhu, X. L. Yang, Y. Zhou, Y. F. Yao, C. Z. Li, *Nanoscale* 2014, **6**, 5971.

48 D. Sarkar, C. K. Ghosh, S. Mukherjee, K. K. Chattopadhyay, *ACS Appl. Mater. Interfaces* 2013*,

5(2), 331.

49 R. Chalasani, S. Vasudevan, *ACS Nano* 2013, **7(5)**, 4093.

50 X. L. Yang, W. Chen, J. F. Huang, Y. Zhou, Y. H. Zhu, C. Z. Li, *Sci. Rep.* 2015, **5**, 10632.